A broader view on EUV-masks: adding complementary imaging modes to the SHARP microscope

Markus P. Benk*[a], Ryan H. Miyakawa [a], Weilun Chao [a], Yow-Gwo Wang [b], Antoine Wojdyla [a], David G. Johnson [a], Alexander P. Donoghue [a], Kenneth A. Goldberg [a]
[a]Lawrence Berkeley National Laboratory, 1 Cyclotron Road, Berkeley, CA 94720, USA
[b]Department of EECS, University of California, Berkeley, CA 94720, USA

ABSTRACT

The authors are expanding the capabilities of the SHARP microscope by implementing complementary imaging modes. SHARP (the SEMATECH High-NA Actinic Reticle review Project) is an actinic, synchrotron-based microscope dedicated to extreme ultraviolet (EUV) photomask research. SHARP's programmable Fourier Synthesis Illuminator and its use of Fresnel zoneplate lenses as imaging optics provide a versatile framework, facilitating the implementation of diverse modes beyond conventional imaging. In addition to SHARP's set of standard zoneplates, we have created more than 100 zoneplates for complementary imaging modes, all designed to extract additional information from photomasks, improve navigation and enhance defect detection. More than 50 new zoneplates are installed in the tool; the remaining lenses are currently in production. In this paper we discuss the design and fabrication of zoneplates for complementary imaging modes and present image data, obtained using Zernike Phase Contrast and different implementations of Differential Interference Contrast.

Keywords: Mask, photomask, EUV, mask imaging, aerial image, zoneplate, Zernike Phase Contrast, Differential Interference Contrast

1. INTRODUCTION

SHARP is designed to emulate image formation in printing tools like the ASML ADT, 3100 and 3300 scanners [1,2] in terms of mask-side numerical aperture (NA), illumination and variation of the plane of incidence across the ring field. The tool's principal application is to collect through-focus data on patterned and blank regions of EUV photomasks, closely emulating a given set of imaging conditions. The data is used to study topics like e.g., printability of defects, evaluation of repairs or 3D-mask effects. SHARP's zoneplate imaging optics match the mask side NA values of current and future lithography generations from (wafer side) 0.25 NA at 6° central ray angle (CRA) up to 0.625 NA at 10° CRA. These NAs are available at different azimuthal angles covering ±25° to emulate the rotation of the plane of incidence. SHARP's Fourier Synthesis Illuminator [3] allows synthesizing arbitrary pupil fills. The flux on the photomask is independent of the fill pattern in use.

Complementary imaging modes allow for extracting additional information from the photomask at an experiment site. In principle, with an increased sensitivity to defects, experiment sites can be found with increased speed and confidence. Previously undiscovered defects can be identified and characterized. Feedback on repairs, beyond printability in a scanner, can be provided.

We have added Zernike Phase Contrast, Differential Interference Contrast, Cubic Phase Modulation, dark-field imaging and stereoscopic imaging to SHARP, most of which are widespread in visible light microscopy. The unique design of the SHARP microscope, using off-axis zoneplate lenses as imaging optics, facilitates the implementation of additional imaging modes and allows, to our knowledge, the first demonstration of Differential Interference Contrast and Zernike Phase Contrast in an EUV optical system. Some of the added imaging modes have very specific illumination requirements, making SHARP's Fourier Synthesis Illuminator a key component to their implementation. An overview of the SHARP microscope and detailed descriptions of its components can be found in Refs. [4,5].

2. ZONEPLATE DESIGN AND FABRICATION

2.1 Zoneplate Design

The common zoneplate equation defines the n-th zone boundary for a standard zoneplate.

$$\frac{n\lambda}{2} + r_p + r_q - p - q = 0 \tag{1}$$

Here, p and q are the imaging conjugates and r_p and are r_q are the distances from the object and image point to a given location in the pupil plane. The wavelength is λ. Figure 1a illustrates the geometry.

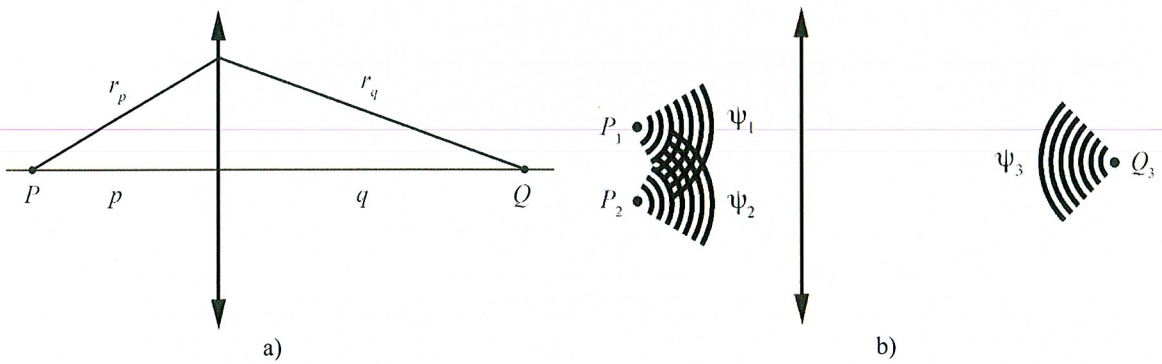

Figure 1. a) Illustration of ray path and statement of symbols used in standard zone pattern definition.
b) Illustration, showing the holographic approach to defining a zone pattern.

For the purposes of fabrication by electron-beam lithography, the authors have written code to generate zoneplate patterns in the Graphic-Database-System format (GDS) from basic inputs like wavelength, imaging conjugates and numerical aperture. The algorithm minimizes position errors in the output file. The code is available to the public at Ref [6]. Zoneplates can be specified via a web interface and the corresponding GDS-file can be downloaded. The site allows calculating resolution and bandwidth requirements for a given configuration and features educational content on the design, fabrication and applications of zoneplate lenses.

A holographic approach is used to define the more complex zone patterns required by some complementary imaging modes. The concept is illustrated in Figure 1 b. For a standard zoneplate we consider an object point P and an image point Q. In the following example we discuss two separate off-axis points P_1 and P_2, imaged to the same image point Q_3. The corresponding waves in the pupil plane are defined in Equation 2.

$$\psi_1 = e^{ikr_1}, \qquad \psi_2 = e^{ikr_2}, \qquad \psi_3 = e^{-ikr_3} \tag{2}$$

Waves ψ_1, ψ_2 and ψ_3 can be combined in different ways in order to obtain an amplitude-only pattern that reflects the geometry given in Figure 1 b. Two approaches are discussed in the following.

The first approach is to sum the waves and calculate the intensity distribution I in the pupil plane.

$$I \propto \left|\psi_1 + \psi_2 + \psi_3\right|^2 \tag{3}$$

This method is akin to the method of recording holograms in light-sensitive film. For e-beam fabrication, the resulting intensity is then *binarized* with a threshold intensity value to obtain a discrete zone pattern. The threshold level can be chosen to maximize a performance metric, such as diffraction efficiency into the twin first orders.

The second approach is to sum the products $\psi_1\psi_3$ and $\psi_2\psi_3$ and threshold its imaginary part f.

$$f = \mathrm{Im}\left(\psi_1\psi_3 + \psi_2\psi_3\right) \tag{4}$$

By itself, the phase of the product $\psi_1\psi_3$ in the pupil plane corresponds to a standard, off-axis zoneplate, imaging P_1 to Q_3. The latter applies to $\psi_2\psi_3$, imaging P_2 to Q_3 as well. Figures 2 a and 2 b show function I and the matching binarized pattern. Function f and its binarized version are shown in Figures 2 c and 2 d. The plots show examples of patterns typically obtained from geometries as presented in Figure 1 b. The equivalence of the two binarized patterns can be explained by the matching center positions of the clear zones. The resulting zoneplates will, however, be different in grating efficiencies in the diffracted orders, and may produce slightly different image qualities. Pattern optimization for non-standard zoneplates is an ongoing topic of investigation. An important aspect to consider is the printability of different patterns in a given lithographic process.

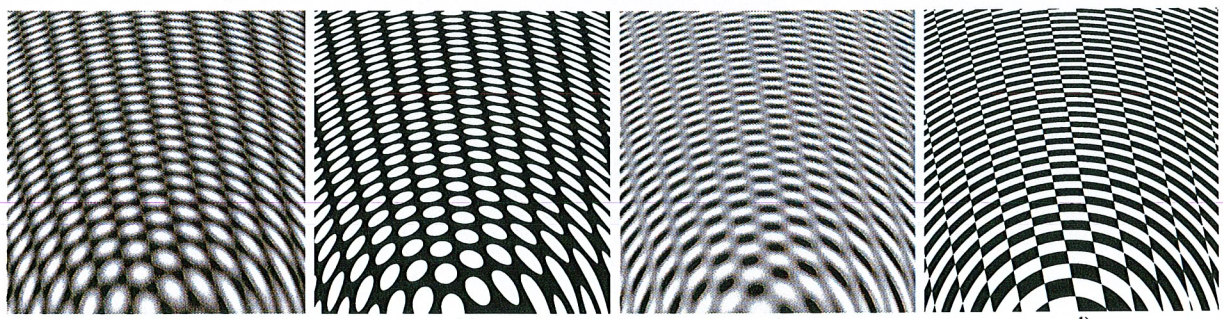

Figure 2. a) Continuous function I from Equation 3. b) Binarized pattern from a). c) Continuous function f from Equation 4. d) Binarized pattern from c).

In order to create GDS-files for non-standard zoneplates with the above approach, the continuous function I or, respectively f, is calculated in the pupil plane at sub-nm resolution. This is done in up to 2500 individual, tiled segments of the pupil to keep the data volume low. A contouring-algorithm is applied to interpolate an outline curve for each clear zone. The outline is then approximated by a polygon, with vertices matching a tolerance of $\lambda/100$ for the optical path length. The polygons from all segments are combined in a single GDS. For zoneplates that contain features smaller than 50 nm, a bias can be applied to the size of the polygons to correct for the size of the e-beam that is used for patterning.

2.2 Zoneplate Nanofabrication

Zoneplates for the SHARP microscope are structured in silicon-nitride membrane windows on silicon chips. Figure 3 a shows an image of SHARP's zoneplate holder with three chips installed. Each chip is kinematically mounted, using three ruby balls that are glued into lithographically etched features on the chips and register to V-shaped grooves in the zoneplate holder. There are more than 200 zoneplates installed in the SHARP microscope. Figure 3 b shows a magnified view of one of the zoneplate chips. Each chip holds approximately 70 zoneplates, grouped on three, 4-mm-long, silicon-nitride membranes, designed to accommodate a large number of zoneplates without compromising robustness and flatness of the membrane.

The individual chips are cut from a 500-μm silicon waver with 100 nm of silicon nitride deposited to both sides. Optical lithography is used to mask the locations of the 3 membranes and the holes for the ruby balls. After removing the upper silicon nitride layer in a dry-etch process, the underlying silicon is etched all the way down to the lower silicon nitride layer to form the 3 membranes. The zone patterns are electroplated in gold using electron-beam lithography. The gold patterns are approximately 40-nm tall. To improve efficiency and reduce the potential effects of carbon contamination, open, elliptical holes are etched through the membrane for the transmitted, illuminating beam. E-beam lithography and dry etch are used to punch holes in the membrane next to each zoneplate. Figure 3 c shows a scanning electron microscopic image of the central part of one of the chips. The image shows 68 individual zoneplates and corresponding holes for the illumination, grouped on three membranes. All zoneplates for additional imaging modes addressed in this article are designed for 6° central ray angle and have a mask-side NA of 0.0825, matching the mask-side NA of the ASML 3300 scanner (0.33 wafer-side NA).

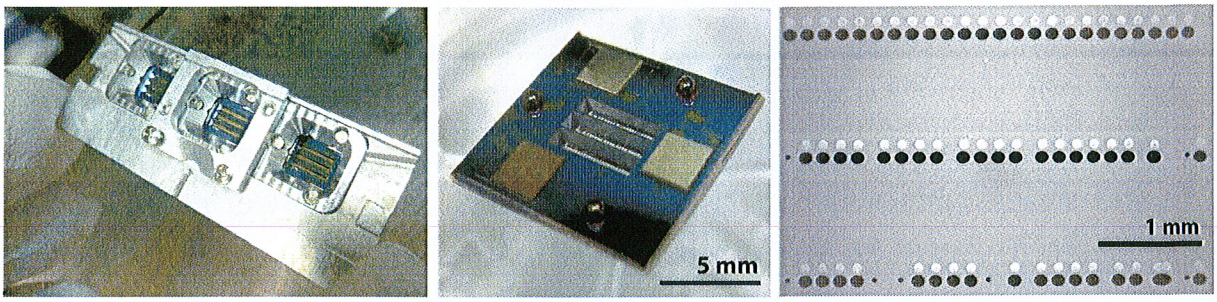

a) b) c)

Figure 3. a) Photographic image of SHARP's zoneplate holder with 3 zoneplate chips installed.
b) Magnified image, showing one of the zoneplate chips.
c) Scanning electron microscopic image of zoneplates and holes on a chip

3. ZERNIKE PHASE CONTRAST

Zernike Phase Contrast is a microscopic technique that enhances contrast by converting phase changes from the object to intensity changes in the image. This is achieved by modifying the phase of the undiffracted light emerging from the object plane and interfering it with the scattered light from the object. The technique is named after Frits Zernike, who developed the technique in the 1930s [7] and was awarded the Nobel Prize in physics for its discovery in 1953.

So-called *phase defects* have long been a major concern in EUV mask technology [8]. In particular nanometer-scale bumps and pits in the reflective coating or the underlying substrate can shift the local multilayer properties and/or modify the optical path of adjacent portions of the reflected field. Despite their potentially strong influence on the EUV aerial image, the detection of pure phase defects can be challenging, even for actinic inspection and imaging tools, because they show little to no contrast in an in-focus bright-field image. Zernike Phase Contrast is widespread in visible-light microscopy for imaging biological samples with low amplitude contrast and strong phase from the varying refractive index and optical path lengths of different materials. We recognize that this technique has the potential to enhance the contrast of phase defects and phase features on EUV masks in a similar way, thus improving the sensitivity of actinic mask-imaging or inspection tools [9].

Zernike Phase Contrast microscopy in the soft x-ray spectral range using a zoneplate lens and phase ring has been demonstrated by Schmahl et al. [10]. With well-collimated illumination, the required phase shift of the undiffracted light can be achieved within the zoneplate pupil, sparing the need for an additional phase-shifting element, and simplifying the design and alignment [11]. Figures 4 a and 4 b show cartoons of a standard, off-axis zoneplate and an off-axis zoneplate for Zernike Phase Contrast, in comparison. To enable Zernike Phase Contrast, the zone pattern is *phase-shifted* in the central part of the pupil. The transition from the unmodified outer region of the zoneplate to the phase-shifted central region is shown in the scanning-electron-microscope (SEM) image in Figure 4 c.

Undiffracted light from the central object plane passes through the phase-shifted region in the center of the zoneplate. Most of the scattered light from a feature or defect passes through the outer region. The two components interfere in the CCD plane, increasing the contrast of object features having a relative phase shift.

Figure 5 a shows SHARP image data, recorded in conventional bright field mode with a pupil fill having a partial-coherence σ value of 0.01 (i.e. highly coherent). The photomask imaged here was provided by the EUV team of GLOBALFOUNDRIES and manufactured at the Advanced Mask Technology Center in Dresden, Germany. It features various sizes of programmed phase defects (bumps and pits) buried under the multilayer.

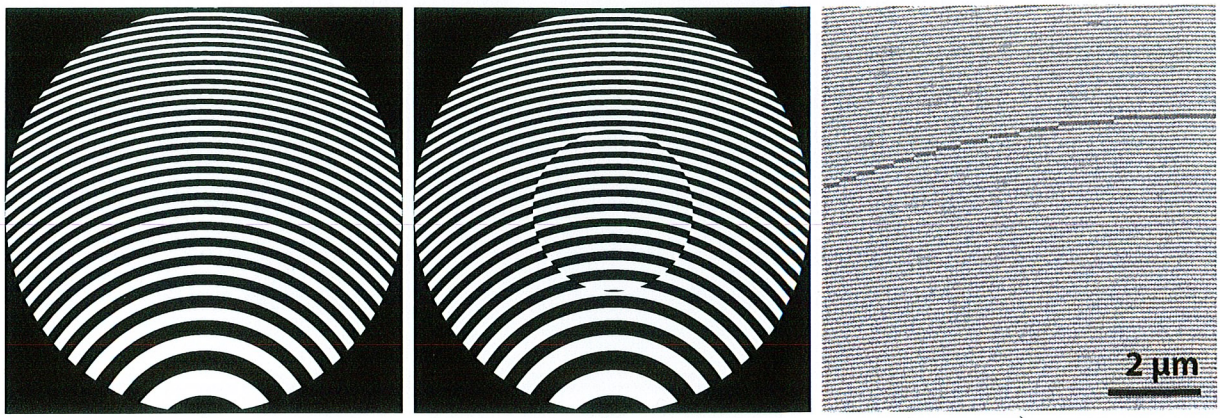

a) b) c)

Figure 4. a) Cartoon of a standard off-axis zoneplate.
b) Cartoon of an off-axis zoneplate for Zernike Phase Contrast.
c) Scanning electron microscopic image of a Zernike Phase Contrast zoneplate, showing the transition from the outer unmodified region of the zoneplate, to the inner phase-shifted region.

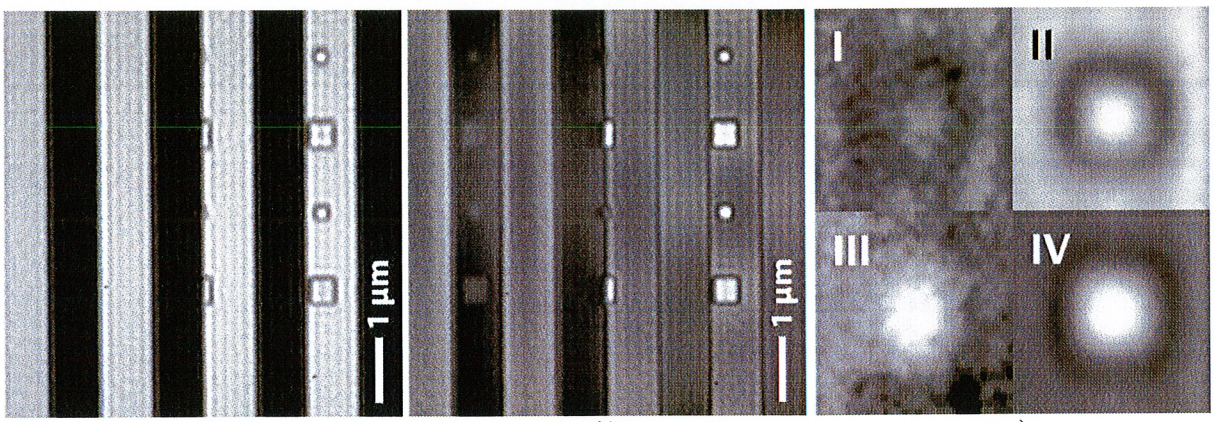

a) b) c)

Figure 5. a) Conventional bright-field image of large phase defects, buried under multilayer
b) Zernike Phase Contrast image of the same location.
c) Magnified and individually scaled images of the defects under absorber and in clear region
I) Bright-field on absorber. II) Bright-field on clear line.
III) Phase contrast on absorber IV) Phase contrast on clear line.

The image shows two large phase defects on the right clear line, resulting from programmed 12-nm-deep pits on the substrate. The larger square features are markers of the defect locations. The off-axis configuration of the SHARP microscope causes a y-direction focal gradient across the image. Here, the lower defect is in focus and contrast occurs at its boundary only. The center of the pit has the same intensity level as the surrounding line. Naturally occurring defects with a more Gaussian profile and less pronounced border show significantly less contrast in focus. The upper defect on the clear line is slightly out of focus – in addition to amplitude contrast from its border, the center of the pit is brighter than the surrounding line. Depending on size and profile, phase defects typically appear bright on one side of focus and dark on the opposite side. Displaying the full extent of intensity levels in the bright-field image (Figure 5 a) on a linear scale, there are no defects visible in the absorber region.

Figure 5 b shows SHARP image data from the same location on the mask, recorded in Zernike Phase Contrast with the same illumination conditions. We observe a reduction in the amplitude contrast from the clear lines to the absorber, and strong phase contrast from the pit to the surrounding bright region. Displaying the image on a linear scale, defects and markers are even visible under the absorber, on the left side of the image. Defect contrast c_{defect} is defined as half the intensity variation across a defect over the arithmetic mean intensity in the image in Equation 5.

$$c_{defect} = \frac{I_{\max}^{defect} - I_{\min}^{defect}}{I_{\max}^{global} + I_{\min}^{global}} \tag{5}$$

For the defect on the clear line, Zernike Phase Contrast increases c_{defect} from 0.695 in conventional bright-field mode to 0.920. For the defect under the absorber, c_{defect} is increased from 0.021 to 0.100. These first results show that Zernike Phase Contrast can significantly increase the signal from phase defects in SHARP image data, thus improving the sensitivity of the microscope. Several factors affect the appearance and observed contrast, including the magnitude of the phase-shift of the central lens region, the radius in the pupil over which the phase shift is applied, the lateral size and phase variation across the defect being observed. Furthermore, it may be useful to apply apodization to balance the amplitudes and optimize the contrast of the interfering elements of the field [9]. Improvements in contrast will be studied for common types of phase, amplitude and combined phase and amplitude defects, found on blank and patterned regions of EUV photomasks.

4. DIFFERENTIAL INTERFERENCE CONTRAST

4.1 Directional DIC

Differential Interference Contrast (DIC) is a microscopic technique originally developed by Georges Nomarski [12]. It is sensitive both to phase and amplitude variation on small length scales in the object plane. Two images of the object are projected onto the image plane with an offset below the resolution limit. Introducing a π phase to one image creates a destructive interference for regions of the image that are spatially uniform in amplitude and phase. Superimposed object points with an initial phase difference show constructive interference, with a maximum value occurring when the relative phase difference is π. Variation in the amplitudes from superimposed points also affect the intensity in the image, thus contributing to contrast. DIC in the x-ray spectral range has been accomplished using twin zone plates [13]. Soft x-ray microscopy in DIC with a single optical element was demonstrated by Chang et al. [14]. The DIC-zoneplates discussed in the following are conceptually similar to the design used in Ref [14]. Figure 6 a and 6 b illustrate zone patterns for DIC in the *x*- and *y*-directions.

Figure 7 a and 7 b show SHARP image data of 175-nm contacts imaged using *y*- and *x*-directional DIC-zoneplates. The size of the contacts is close to the resolution limit of the 0.33 4xNA zoneplates. Thus the image of a contact closely resembles the point spread function. Figure 7 c shows the phase of the simulated complex electric field in the image plane, multiplied by the amplitude, for a point-like object. The point spread functions of the DIC-zoneplates have two maxima, and in the center, the intensity is zero. The two maxima differ in phase by π, as can be seen in Figure 7 c. The point spread function resembles the discrete derivative operator D_x=[-1 0 1]: the *x*-derivative is applied to the image. In the center of the images, the power is balanced in the two maxima. Outer parts of the object field display some imbalance in power. The amplitude of a wave, emerging from an ideal point source is constant in power. The 175-nm contacts are expanded objects that project a diffraction pattern into the pupil. For plane-wave illumination, the distribution of power within the pupil depends on the location of the contact within the object field. For contacts in the centerline of the object field, perpendicular to the direction of the DIC, the power is distributed evenly between the two different sides of the pupil. With increasing distance to the centerline, the imbalance in power across the two sides of the pupil causes an increasing bright-field contribution added to the DIC image.

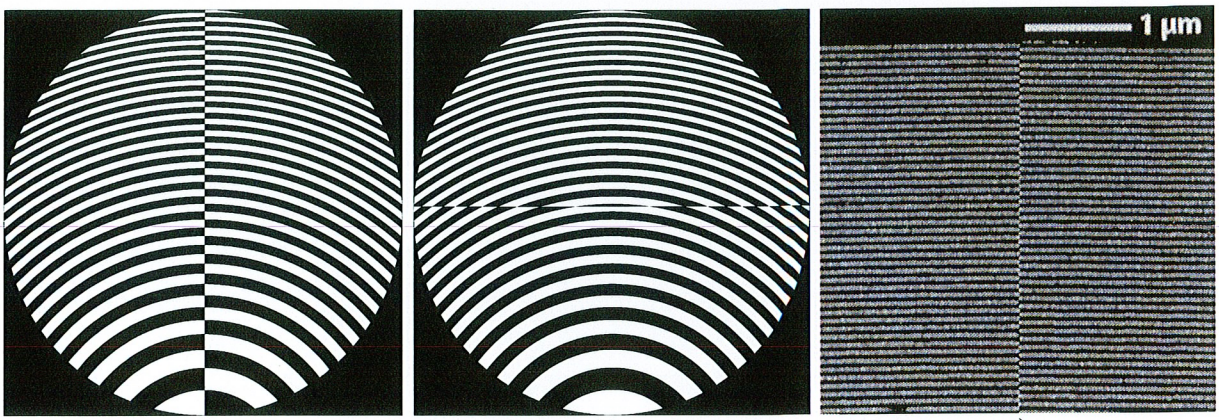

Figure 6. a) Cartoon of an *x*-directional DIC-zoneplate lens.
b) Cartoon of a *y*-directional DIC-zoneplate lens.
c) SEM image of an *x*-directional DIC-zoneplate lens, showing the phase shift in the pattern along the horizontal center of the aperture at the upper edge where the zones are smallest.

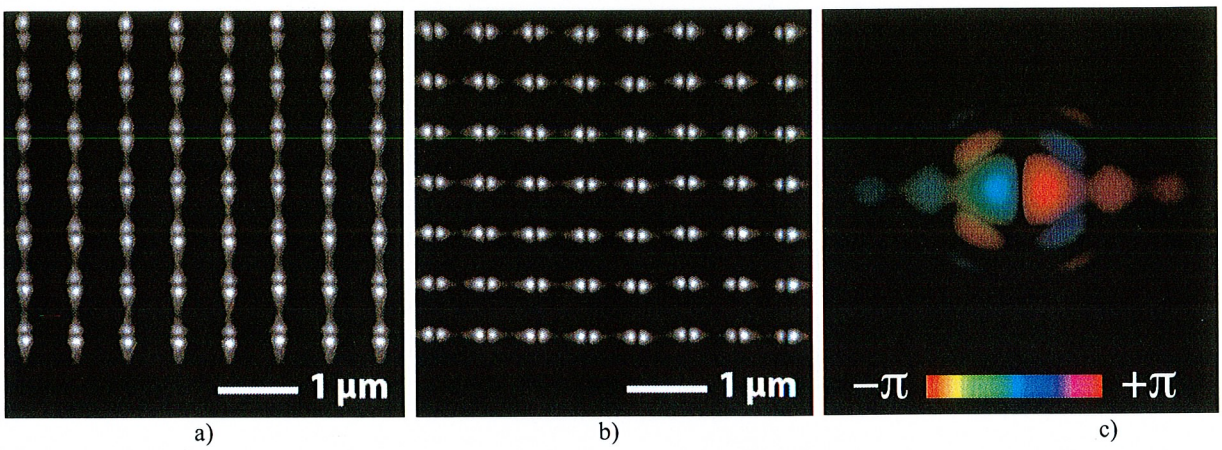

Figure 7. SHARP EUV image details, showing 175-nm loose-pitch contacts, imaged with a DIC-zoneplates.
a) *y*-directional DIC b) *x*-directional DIC.
c) Magnified false color image, showing the phase of the simulated complex electric field in the image plane, multiplied by the amplitude, for a point-like object, imaged with the *x*-directional DIC-zoneplate.

4.2 Isotropic DIC

The Radial Hilbert Transform constitutes another differential contrast enhancing technique. It provides an isotropic measurement of the amplitude and phase gradient in a sample [15]. The technique has been implemented, adding a vortex-like phase plate H_p of the form $H_p(r,\phi) = \exp(i\,P\phi)$ to the back focal plane of an imaging system [16]. The phase plate retards the phase by P–times 2π along its circumference. Combination of phase modification and focusing power in a single optical element is demonstrated in Ref. [15] for the soft x-ray spectral range. The latter concept is implemented in SHARP, using spiral zone plates of the orders P=1 and P=3 in an off-axis configuration.

a) b) c)

Figure 8. a) Cartoon of an on-axis spiral zoneplate of the order P=1.
b) Cartoon of a spiral zoneplate of the order P=1 in off-axis configuration.
c) Cartoon of a spiral zoneplate of the order P=3 in off-axis configuration.

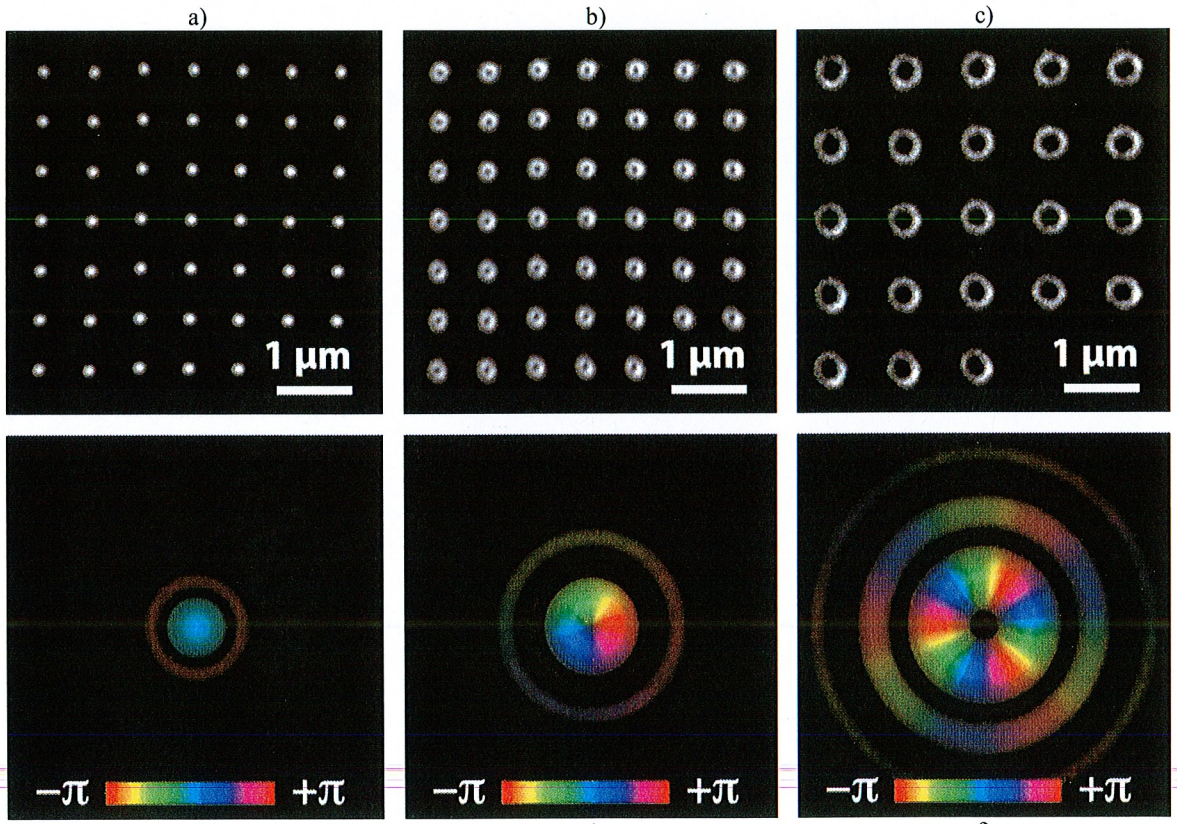

Figure 9. a) SHARP image data showing 175-nm contacts, imaged using a standard zoneplate.
b) SHARP image data showing 175-nm contacts, imaged using a spiral zoneplate of the order P=1.
c) SHARP image data showing 175-nm contacts, imaged using a spiral zoneplate of the order P=3.
d) Magnified simulated false color image, showing the phase of the complex electric field in the sensor plane, multiplied by the amplitude, generated by a point-like object, for a standard zoneplate.
e) Same as d), but for a spiral zoneplate of the order P=1.
f) Same as d), but for a spiral zoneplate of the order P=3.

Figure 8 a illustrates the pattern of an on-axis spiral zoneplate of the order P=1. Patterns of spiral zoneplates of the order P=1 and P=3 in off-axis configuration are illustrated in Figures 8 b and 8 c. Figures 9 b and 9 c show SHARP image details of 175-nm contacts, imaged using spiral zoneplates. The zoneplates produce ring-shaped point spread functions. For the contacts, shown in Figure 9 c, a looser pitch was chosen to prevent overlapping. The calculated change in phase along the circumference of the point spread function can be seen in Figures 10 e and 10 f, showing the phase of the simulated electric field in the image, multiplied by the amplitude, for a point-like object imaged with spiral zoneplates of the order P=1 and P=3. A conventional image of 175-nm contacts and the phase of the corresponding simulated electric field are shown in Figures 9 a and 9 d as a reference.

4.3 DIC Image Data

Figure 10 shows SHARP image details of 400-nm elbows recorded in different imaging modes, for comparison.

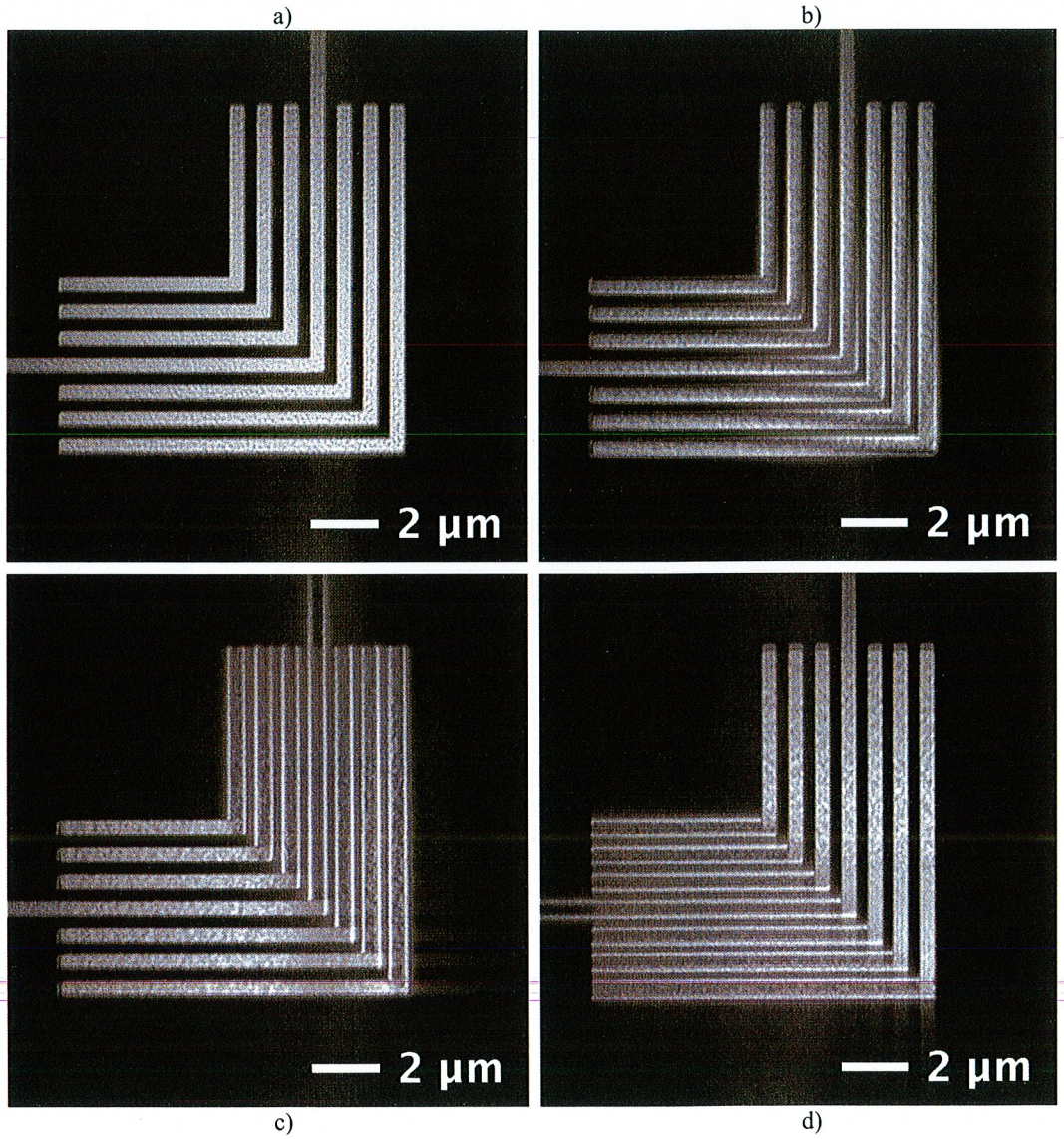

Figure 10. SHARP image details of 400-nm half-pitch elbows under coherent illumination.
a) Conventional bright-field mode. b) Spiral zoneplate of order P=1.
c) x-directional DIC. d) y-directional DIC.

All of the images were recorded with a pupil fill of σ=0.01. A conventional bright field image is shown in Figure 10 a as a reference. The image in Figure 10 b was recorded using a spiral zoneplate of the order P=1. The image shows relief-like contrast and edge enhancement in the sweet spot of the lens. The granularity caused by substrate roughness is enhanced, compared to the bright field image. Figure 10 c shows x-directional DIC imaging. The central vertical line of the elbow pattern shows clear, x-derivative characteristics. The signal is high at the edges and drops to a low value inside the clear line. With increasing distance from the center axis, in addition to signal at the edges of the lines, there is bright-field contribution visible in the clear lines. The granularity is minimized close to the center axes and enhanced in both vertical and horizontal lines away from the center axis. The y-directional DIC image shows similar properties.

5. SUMMARY AND OUTLOOK

We have demonstrated the addition of complementary imaging modes to the SHARP EUV mask microscope, in an effort to extract additional information from actinic photomask imaging, improve navigation and enhance defect detection. Zernike Phase Contrast has been implemented in an actinic EUV mask-imaging tool for the first time and is available to users of SHARP. Early results show significantly enhanced signal from phase defects. Differential Interference Contrast in the x and y directions and isotropic DIC have been demonstrated. The latter techniques increase contrast on a variety of features, including phase defects and intensity speckle from substrate and multilayer roughness. Further activity will be directed at demonstrating the effectiveness of Zernike Phase Contrast and Differential Interference Contrast in real-world defect detection and classification. Cubic Phase Modulation, dark-field imaging and stereoscopic imaging are further imaging modes that have been added to the tool, and will be discussed in further publications. A second chip with zoneplates for additional complementary imaging modes is currently in production.

6. ACKNOWLEDGEMENT

The Advanced Light Source at Lawrence Berkeley National Laboratory is supported by the Director, Office of Science, Office of Basic Energy Sciences, of the U.S. Department of Energy under Contract No. DE-AC02-05CH11231. We gratefully acknowledge SEMATECH funding of the SHARP microscope, and Anne Rudack the SHARP project manager. Test masks used in imaging experiments described above were provided by GlobalFoundries and Intel.

REFERENCES

[1] Peeters, R. et al., "EUV lithography: NXE platform performance overview", Proc. SPIE 9048, 90481J (2014).
[2] Wagner, C. et al., "EUV into production with ASML's NXE platform", Proc. SPIE 7636, 76361H (2010).
[3] Naulleau, P. P., Goldberg, K. A., Batson, P., Bokor, J., Denham, P. and Rekawa, S., "Fourier-synthesis custom-coherence illuminator for extreme ultraviolet microfield lithography", APPLIED OPTICS 42(5), 820-826 (2003).
[4] Goldberg, K. A. et al, "Actinic mask imaging: Recent results and future directions from the SHARP EUV Microscope", Proc. of SPIE Vol. 9048, 90480Y (2014).
[5] Goldberg, K. A. et al, "Commissioning an EUV mask microscope for lithography generations reaching 8 nm", Proc. of SPIE Vol. 8679, 867919 (2013).
[6] Miyakawa, R. H., Anderson, C. N. and Naulleau, P. P., "Zone plate education, design, tolerancing, fabrication, and applications.", Lbl, 10 September 2014, <http://zoneplate.lbl.gov> (24 September 2014). http://zoneplate.lbl.gov
[7] Zernike, F., "Phase contrast, a new method for the microscopic observation of transparent objects", Physica 9(7), 686-698 (1942).
[8] Nguyen, K. P., Wong, A. K., Neureuther, A. R. and Attwood, D. T., "Effect of absorber topography and multilayer coating defects on reflective masks for soft x-ray/EUV projection lithography", Proc. of SPIE Vol. 1924, 418-434 (1993).
[9] Wang, Y. G., Miyakawa, R. H., Neureuther, A. R. and Naulleau, P. P., "Zernike phase contrast microscope for EUV mask inspection", Proc. SPIE 9048, 904810 (2014).
[10] Schmahl, G., Rudolph, D., Guttmann, P., Schneider, G., Thieme, J. and Niemann, B., "Phase contrast studies of biological specimens with the xray microscope at BESSY", Review of Scientific Instruments 66, 1282 (1995)
[11] Sakdinawat, A. and Liu, Y., "Phase contrast soft x-ray microscopy using Zernike zone plates", OPTICS EXPRESS, 16(3), 1559-1564 (2008).

[12] Nomarski, G., "Microinterferometrie differential a ondes polarisés," J. Phys. Radium 16, 9-135 (1955).
[13] Kaulich, B., Wilhein, T., Di Fabrizio, E., Romanato, F., Altissimo, M., Cabrini, S., Fayard, B. and Susini, J., "Differential interference contrast x-ray microscopy with twin zone plates", J. Opt. Soc. Am. A, 19(4), 797-806 (2002).
[14] Chang, C., Sakdinawat, A., Fischer, P., Anderson E. and Attwood, D., "Single-element objective lens for soft x-ray differential interference contrast microscopy", OPTICS LETTERS 31(10), 1564-1566 (2006).
[15] Sakdinawat, A. and Yanwei, L., "Soft-x-ray microscopy using spiral zone plates", OPTICS LETTERS 32(18), 2635-2637 (2007).
[16] Davis, J. A., McNamara, D. E., Cottrell D. M. and Campos, J., "Image processing with the radial Hilbert transform: theory and experiments", OPTICS LETTERS, 25(2), 99-101 (2000).

DISCLAIMER

This document was prepared as an account of work sponsored by the United States Government. While this document is believed to contain correct information, neither the United States Government nor any agency thereof, nor The Regents of the University of California, nor any of their employees, makes any warranty, express or implied, or assumes any legal responsibility for the accuracy, completeness, or usefulness of any information, apparatus, product, or process disclosed, or represents that its use would not infringe privately owned rights. Reference herein to any specific commercial product, process, or service by its trade name, trademark, manufacturer, or otherwise, does not necessarily constitute or imply its endorsement, recommendation, or favoring by the United States Government or any agency thereof, or The Regents of the University of California. The views and opinions of authors expressed herein do not necessarily state or reflect those of the United States Government or any agency thereof or The Regents of the University of California.